Journal of
Materials Chemistry B

Materials for biology and medicine

Accepted Manuscript

This article can be cited before page numbers have been issued, to do this please use: D. Bhardwaj, V. Chawla, V. Nandwani, Y. Thakur, Y. Singh and G. Agrawal, *J. Mater. Chem. B*, 2025, DOI: 10.1039/D5TB00800J.

ROYAL SOCIETY OF CHEMISTRY

rsc.li/materials-b

View Article Online
DOI: 10.1039/D5TB00800J

Multifunctional Electrospun Nanofiber/Hydrogel-based Pro-healing Bilayer Dressings as Next Generation Biomaterial for Skin Wound Care

Dimpy Bhardwaj,[a] Vatan Chawla,[b] Vanshika Nandwani,[a] Yashika Thakur,[b] Yashveer Singh,[b] and Garima Agrawal[a,*]

[a]School of Chemical Sciences and Advanced Materials Research Centre, Indian Institute of Technology Mandi, Mandi-175075, Himachal Pradesh, India

[b]Department of Chemistry, Indian Institute of Technology Ropar, Rupnagar-140001, Punjab, India

*Correspondence: garima@iitmandi.ac.in; Tel.: +91-1905-267827; https://orcid.org/0000-0002-3391-2378

Abstract

Infectious wounds present a significant challenge in healthcare due to the delay in wound healing and associated processes. Improper use of antibiotics makes this situation even worse due to antibiotic resistance. To meet the critical requirements of healing infectious wounds, we report a bilayer dressing (BL) that combines a hydrogel-based layer and an electrospun nanofiber-based layer together to mimic the dermal and epidermal architecture of normal skin. The bilayer dressing is fabricated by combining chitosan/gelatin nanofiber-based layer (NF) with ursodeoxycholic acid drug (UDC) and carbon dots (CDs) loaded hydrogel (UDC/CDs/H-Gel). Hydrogel is fabricated by Schiff base-based crosslinking of quaternized chitosan (QCS) and oxidized alginate (OA). The integration of NF with UDC/CDs/H-Gel leads to ~45% increment in tensile strength and ~48% increment in elongation at break. BL exhibits swelling of ~400% in 36 h, porosity of ~75%, and antioxidant activity of ~93%. Moreover, as compared to individual NF and hydrogel layer, BL shows good reactive oxygen species (ROS) scavenging behavior, hemocompatibility (~4.5% hemolysis), good hemostatic potential, enhanced cell proliferation ability (130% cell viability of L929 cells), and excellent antibacterial activity with 92% and 88% bactericidal efficacy against *E.*

View Article Online
DOI: 10.1039/D5TB00800J

coli and *S. aureus*, respectively. Wound healing ability of BL is further evaluated via scratch assay demonstrating ~97% wound closure. Overall, BL possesses multifunctionality, and presents itself as a potential candidate for accelerated wound healing.

Keywords: Electrospinning, nanofibers, hydrogel, bilayer dressing, carbon dots, antibacterial, wound healing

Introduction

Skin is the outermost layer of the body that directly comes into contact of the environment, and it is one of the most vulnerable tissue due to its closest interaction with the external factors. For minor injuries, skin can heal itself over time via a complex wound healing process, which includes four overlapping and coordinated stages, namely hemostasis, inflammation, proliferation, and remodeling.[1, 2] This process helps in restoring the overall physiology and function of skin but any kind of disruption in this continuous healing process may lead to chronic wounds having persistent inflammation and impaired healing. Various factors, like diabetes, infection, and stress interfere with wound healing process, resulting in higher occurrence of chronic wounds.[2, 3] According to a study, wound care related expenditure is estimated to be around $28 billion - $97 billion annually, resulting in heavy financial burden in the medical sector.[4]

Gauze is the most traditional and inexpensive alternative to treat the wound but the need for their frequent replacement may lead to trauma and mechanical debridement, and the leftover fiber may trigger the immune system causing granuloma formation.[5] To address this challenge, advanced wound dressings have been designed based on “the moist wound healing theory” given by Prof. Winter in 1962.[6] An ideal wound dressing is expected to be biocompatible and non-inflammatory; retain moisture; and have sufficient mechanical strength to maintain the structural integrity. It should be capable of performing the required biochemical actions for supporting the healing process.[7]

Various monolayer wound dressings based on hydrogels, electrospun fibers, foams, and hydrocolloids have been investigated to address the challenges associated with gauze.[8-11] To design the polymer matrix for these wound healing dressings, natural polymers are an attractive choice owing to their inherent biocompatibility and biodegradability.[12-14] These natural polymers, such as chitosan, alginate, gelatin can be extracted from natural resources and possess different functional groups, which can be used for post-modifications as per the requirements.[15-17] In recent years,

View Article Online
DOI: 10.1039/D5TB00800J

hydrogels loaded with nanomaterials have attracted considerable interest for wound healing applications.[18-21] In this context, silver-based nanomaterials have been widely utilized for the treatment of infected wounds due to their strong and broad-spectrum antibacterial efficacy.[22] However, apprehensions regarding their cytotoxic effects on host tissues and the risk of inducing allergic reactions have limited their utilization.[23] In recent years, carbon dots have emerged as an alternative active component owing to their exceptional biocompatibility, intrinsic antioxidant property, adjustable surface functionalities, and antibacterial efficacy combined with minimum toxicity risk.[24, 25] For example, Zaffar *et al.* developed urea/citric acid-based carbon dots and rose-petal-derived extracellular vesicles loaded injectable hydrogel with intrinsic antibacterial activity.[26] Qu *et al.* reported MXene/carbon dots nanocomposites with anti-inflammatory and NIR-triggered antibacterial effects.[27] Further, Li *et al.* incorporated peroxidase-like copper-doped carbon dots into a chitosan/dextran-based hydrogel for stimuli-responsive biofilm disruption and enhanced healing.[28] The above mentioned systems have required features for wound healing applications exclusive of each other, but, none of the systems independently attain the complete set of physical and biological efficacy when used as an individual layer.

The development of porous dressings with layered gradient can be considered as a step further, as it mimics the skin anatomy, which has epidermis and dermis.[29] In this regard, bilayer (BL) dressings consisting of electrospun fiber-based layer and hydrogel-based layer have emerged as a potential alternative.[4, 30-32] Here, electrospun fiber-based layer provides the dense structure with small pores to maintain the breathability and providing protection from bacterial invasion, which is similar to epidermis,[4, 33] whereas, the loose 3D porous structure of hydrogel layer can mimic the dermal layer by providing the moist environment and supporting cell growth along with offering other required biochemical functions.[4, 34] However, relatively limited studies have been performed so far on bilayer dressings. Bilayer dressings based on cellulose acetate nanofibers with collagen hydrogel,[35] poly(L-lactic acid) (PLLA) nanofibers with chitosan/gelatin hydrogel,[4] PLLA/chitosan/poly(3-hydroxybutyrate-co-3-hydroxyvalerate) (PHBV) nanofibers with chitosan/gelatin hydrogel,[36] keratin nanofibers with polyacrylic acid hydrogel,[32] and polyvinyl alcohol/alginate nanofibers with chitosan hydrogel[37] are some examples that have been reported in the literature. These bilayer dressings generally lack the capability of performing multiple actions together like antioxidant, antibacterial, controlled release of active components, hemostasis, and reactive oxygen species (ROS) scavenging, which is crucial for the healing of

View Article Online
DOI: 10.1039/D5TB00800J

infectious wounds. Therefore, it is the need of the hour to focus on multifunctional bilayer dressings for achieving faster healing of bacteria-infected wounds, and to improve their prospects in real-life applications.

To address research gap of desired multifactorial physical and biological properties in a single dressing, based on the above-mentioned knowledge, we hypothesized to combine chitosan/gelatin-based electrospun fibers with ursodeoxycholic acid drug (UDC) and citric acid-based carbon dots (CDs) loaded hydrogel. UDC shows strong potential for promoting wound healing due to its ability to suppress NF-κB signaling, along with its anti-inflammatory effects and tissue regeneration feature.[38, 39] Here, polymeric matrix with UDC can help in wound exudate absorption, cell adhesion and proliferation, and hemostasis, while chitosan and CDs can offer antioxidant, antibacterial, and ROS scavenging features. Also, good interfacial adhesion of nanofibers and hydrogel-based layers can offer enhanced mechanical strength to the dressing. Based on this hypothesis, in the current work, we have developed bilayer dressings fabricated by combining chitosan/gelatin-based electrospun fibers with quaternized chitosan/alginate-based hydrogel for enhanced wound healing. The epidermis-mimicking layer was prepared by electrospinning the solution of chitosan and gelatin, whereas dermis-mimicking hydrogel layer was prepared by Schiff base-based crosslinking between quaternized chitosan (QCS) and oxidized alginate (OA). Hydrogel layer was further loaded with CDs and UDC, thus providing the antioxidant, antibacterial, and cell growth promoting features to the bilayer dressing. These bilayer dressings (BL) were investigated for their various physicochemical and active properties. The wound healing ability of BL was investigated through *in vitro* scratch assay, which revealed a substantial decrease in the scratch area. Owing to their biochemical functions, the developed bilayer dressings demonstrate great potential as a dressing material for enhanced wound healing.

2. Materials and methods

2.1. Materials

Chitosan (600-800 kDa mol. wt.), sodium hydroxide (NaOH, 97%), 3-(4,5-dimethylthiazol-2-yl)-2,5- diphenyl-2H tetrazolium bromide (MTT), Dulbecco's modified Eagle's medium (DMEM), fetal bovine serum (FBS), Triton-X and RPMI were purchased from Thermo Fisher Scientific, India. Gelatin Type A (Total nitrogen ≥15.50 %, Protein: 70-90 %) and Luria broth were purchased from HiMedia, India. Sodium alginate (Alg, ~200 kDa mol. wt.) was acquired from CDH, India. Sodium metaperiodate (99.8 %), phosphate buffer saline (PBS), and ethylene glycol (99.5%) were

View Article Online
DOI: 10.1039/D5TB00800J

purchased from Loba Chemie, India. Glycidyl trimethyl ammonium chloride (ca. 80% in water), ursodeoxycholic acid (UDC, >98.0 %), and 2,2-diphenyl-1-picrylhydrazyl radical (DPPH) were acquired from TCI chemicals, India. Citric acid (≥99.0 %) and 2′,7′- dichlorodihydrofluorescein diacetate (H_2DCFDA, ≥ 97 %) were acquired from Merck Life Science, India. Acetic acid (99.0 %), p-nitrophenylhydrazine (99 %), dimethylformamide (DMF, 99.5 %), and ethylene diamine (99 %) were purchased from SRL, India. *S. aureus* (MTCC 7443) and *E. coli* (MTCC 1687) were obtained from CSIR - IMTECH, Chandigarh. Fresh human blood was collected from healthy human, following the guidelines approved by the Institutional Biosafety Committee (#07/2021-II/IIT/IEC).

2.2. Fabrication of citric acid-based carbon dots (CDs)

CDs were prepared using citric acid as the source of carbon via one-step hydrothermal method.[40, 41] Briefly, 2.5 g of citric acid and 2.5 mL of ethylene diamine were mixed together in 50 mL of water, and the solution was transferred to teflon lined stainless steel reactor (100 mL). The reaction was carried out at 180 °C for 12 h. Next, sample was centrifuged at 8000 rpm min^{-1} for 10 min and then filtered through a 0.22 μm membrane filter. Finally, the sample was dialyzed against water for 48 h using 1 kDa dialysis membrane, and stored at room temperature.

2.3. Fabrication of chitosan/gelatin electrospun nanofiber-based layer (NF)

To fabricate NF, 8% w/v chitosan solution was prepared in 3 mL of 80% acetic acid, and 30% w/v gelatin solution was prepared separately in 6 mL of 80% acetic acid. Both solutions were mixed and kept for overnight stirring until the mixture was homogenous and viscous, and this uniform solution was electrospun over the cylindrical collector positioned 15 cm away, perpendicular to needle. Needle was attached to the positive terminal of a high-voltage direct current power supply and nanofibers were collected by applying an electric potential of 16 kV to the polymer solution, with flow rate of 0.4 mL/h.

2.4. Formation of bilayer dressing (BL)

To fabricate BL, QCS and OA were utilized to generate Schiff base linkage-based hydrogel layer. QCS was prepared according to the methodology reported by Negi *et al,*[42] and the degree of quaternization (~23%) was estimated by conductometric titration using the following formula:

$$\frac{C_{AgNO_3} \cdot V_{AgNO_3}}{m} = \frac{DS}{DS \cdot M_3 + (1 - DS - DA) \cdot M_1 + DA \cdot M_2} \quad \textbf{Equation 1}$$

View Article Online
DOI: 10.1039/D5TB00800J

where, C_{AgNO_3} = $AgNO_3$ concentration, V_{AgNO_3} = volume of $AgNO_3$ solution, m = mass of QCS used for titration, DS is the degree of quaternization, DA is the acetylation degree of chitosan, M_1 = glucosamine molecular weight, M_2 = N-acetyl glucosamine molecular weight, and M_3 = GTMAC molecular weight.

OA was synthesized using the previously described protocol by Dhiman *et al.,*[43] and the hydroxylamine hydrochloride assay was used to calculate percent oxidation (~71%) using following formula:

$$\frac{Mole\ of\ CHO}{Mole\ of\ Uronic\ acid} = V_{NaOH} \times 0.1 molL^{-1} \times \frac{198 gmol^{-1}}{M_{sample}} \times 100 \qquad \textbf{Equation 2}$$

here, V_{NaOH} represents the volume of NaOH consumed during titration, and M_{sample} denotes the mass of oxidized alginate used in the titration.

In the next step, 150 µL of QCS solution and 150 µL of OA solution in DI water were mixed homogeneously by maintaining QCS:OA ratio of 3:5 (w/w). Next, CDs (1:80 w/w relative to hydrogel forming solution) and methanolic solution of UDC (1:10 w/w relative to hydrogel forming solution) were added to the aforementioned solution.

Finally, bilayer dressing was prepared by using the vacuum filtration method, where NF was kept in the Buchner funnel and hydrogel forming solution was poured onto it. It was observed that hydrogel layer was formed within 2 min at room temperature, and after applying vacuum, strong interface between the two layers was formed that can be clearly visualized using SEM. BL were characterized using FT-IR spectroscopy, SEM and universal testing machine (UTM).

For comparative studies, following hydrogel samples were prepared: (a) unloaded QCS/OA hydrogel (H-Gel) and (b) UDC and CDs loaded QCS/OA hydrogel (UDC/CDs/H-Gel). Loading efficiency of UDC drug was calculated as follows:[44]

$$\%\ Loading\ efficiency\ (LE) = \frac{Amount\ of\ drug\ added}{Weight\ of\ film} \times 100 \qquad \textbf{Equation 3}$$

2.5. Physicochemical characterizations and *in vitro* studies

The experimental details of physicochemical characterization, UDC release studies, antioxidant and antibacterial studies, and cell studies are given in the **Supporting Information.**

2.6. Instrumentation and characterization

The details of instrumentation and characterization are given in the **Supporting Information.**

3. Results and discussion

View Article Online
DOI: 10.1039/D5TB00800J

In this work, bilayer dressing (BL) was designed to deal with the challenges related to infectious wounds while keeping the bilayer structure of skin in mind. Chitosan/gelatin electrospun nanofiber-based layer (NF) was prepared separately using electrospinning method. Next, bilayer dressing (BL) was developed by pouring CDs and UDC containing hydrogel forming solution on NF under vacuum filtration (**Scheme 1**). Here, hydrogel layer was formed on top of NF and a strong interface was formed between NF and hydrogel layer resulting in bilayer structure, offering multifactorial pro-healing features for enhanced skin wound healing.

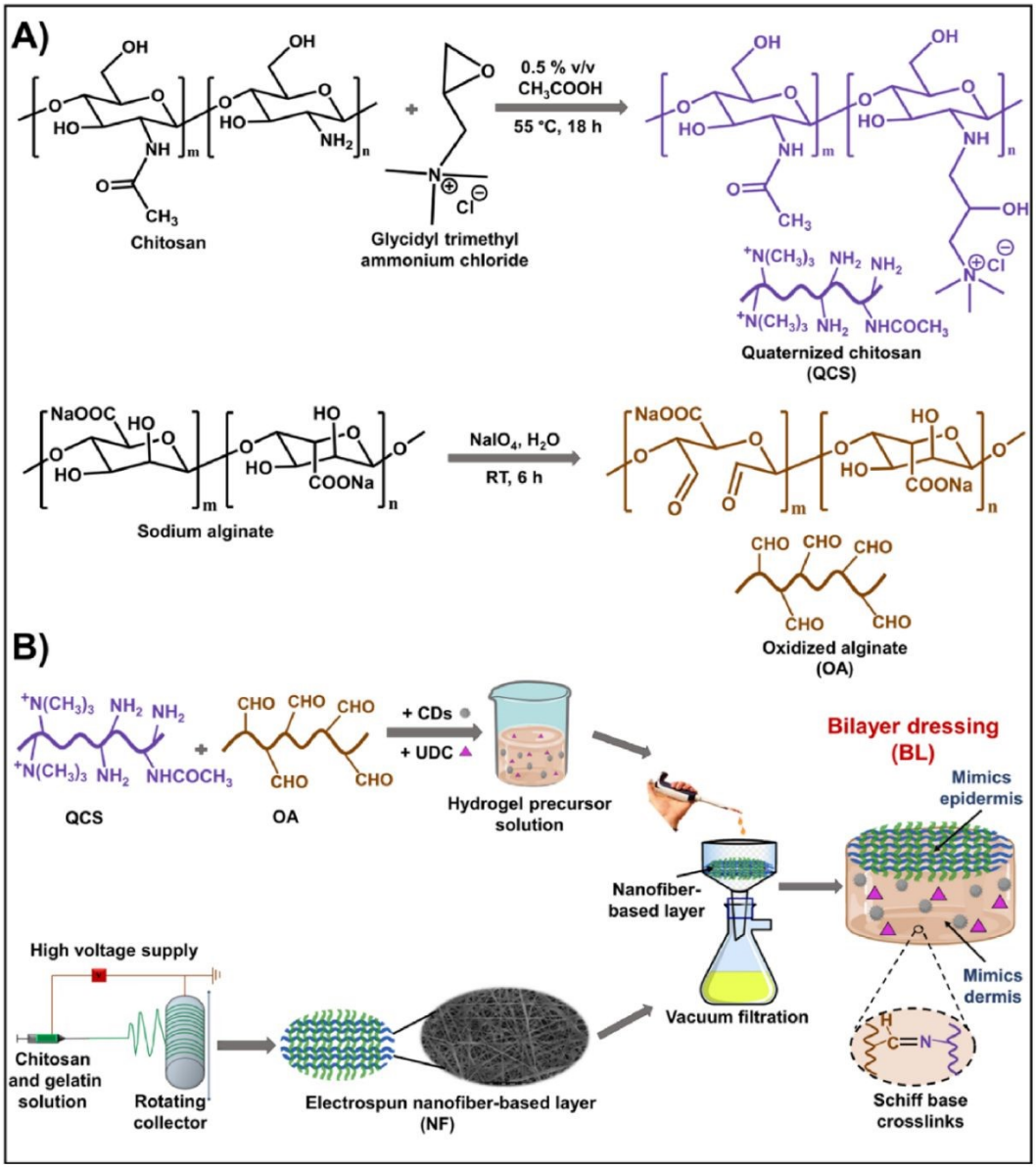

View Article Online
DOI: 10.1039/D5TB00800J

Scheme 1. (A) Synthesis of quaternized chitosan (QCS) and oxidized alginate (OA). (B) Fabrication of multifunctional electrospun nanofiber/hydrogel-based pro-healing bilayer dressing (BL) for infectious wounds.

3.1. Characterization of chitosan/gelatin electrospun nanofiber-based layer (NF)

Chitosan/gelatin electrospun nanofiber-based layer was fabricated via electrospinning method. A comparative FT-IR spectra of chitosan, gelatin, and NF is shown in **Figure S1** in **Supporting Information**. It can be seen that all the peaks of gelatin and chitosan were present in the FT-IR spectrum of NF confirming the presence of both the biopolymers in the nanofibers. These fibers are expected to have hydrogen bonding interactions between $–NH_2$, –C=O, and –OH groups of both chitosan and gelatin. Similar interactions have also been reported in other chitosan/gelatin-based systems in the literature.[45] Fabricated NF was also characterized using SEM and the results have been discussed later in **section 3.4**.

3.2. Characterization of citric acid-based carbon dots (CDs)

CDs were prepared via one-step hydrothermal method utilizing citric acid as a carbon source. CDs displayed a size of 28 nm with the polydispersity index (PDI) of 0.3 as measured by dynamic light scattering (**Figure S2**, **Supporting Information**). Zeta potential of CDs was -23.6 mV indicating the colloidal stability of CDs via strong electrostatic repulsion (**Figure S3**, **Supporting Information**). TEM image of CDs exhibited their homogeneous distribution (**Figure 1A**) with average size of approximately 4.2 ± 1.9 nm (**Figure 1B)**.

FT-IR spectra of citric acid and CDs are shown in **Figure S4** in **Supporting Information**. FT-IR spectrum of citric acid showed peaks at 3492 cm^{-1} (O–H stretching) and 3280 cm^{-1} (O–H stretching of carboxylic group), 2892 cm^{-1} (C–H stretching), and 1697 cm^{-1} (C=O stretching), whereas FT-IR spectrum of CDs displayed peaks at 3284 cm^{-1} (O–H and N–H stretching), 2930 cm^{-1} (C–H stretching), 1540 cm^{-1} (asymmetric C–O stretching of carboxylate group), and 1370 cm^{-1} (symmetric C–O stretching of carboxylate group). A peak at 1580 cm^{-1} (N–H bending) was also observed in the case of CDs, which was attributed to the nitrogen functionalities on CDs.[43, 46]

View Article Online
DOI: 10.1039/D5TB00800J

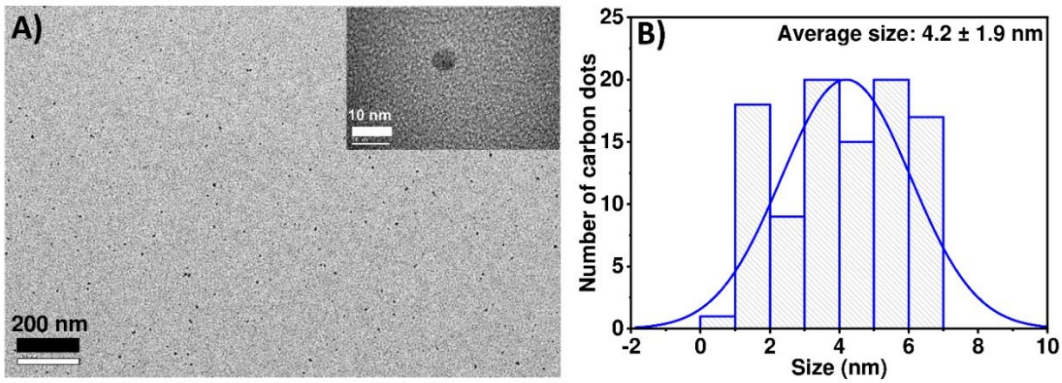

Figure 1. (A) TEM image of CDs, scale bar: 200 nm. Inset displays the TEM image of a single CD with scale bar as 10 nm. (B) Histogram showing size distribution of CDs.

Moreover, X-ray photoelectron spectral (XPS) analysis was performed to detect the surface components and functional groups in CDs. XPS survey spectrum for CDs displayed the presence of carbon, oxygen, and nitrogen elements in CDs (**Figure S5A, Supporting Information**). High-resolution spectrum of C1s exhibited three peaks (**Figure S5B, Supporting Information**) at 288 eV, 286.3 eV, and 284.7 eV, which were ascribed to C=O, C–N, and C–C, respectively.[47] N1s spectrum indicated the presence of alkyl ammonium groups (401.8 eV) and N–H (399.6 eV) groups, thus, demonstrating the presence of nitrogen containing functionalities on CDs (**Figure S5C, Supporting Information**).[48] Moreover, O1s spectrum was deconvoluted into two peaks revealing the presence of C–O (532.9 eV) and C=O (531.5 eV) (**Figure S5D, Supporting Information**).[40] These XPS results are in good agreement with FT-IR results.

3.3. Characterization of UDC and CDs-loaded QCS/OA hydrogel (UDC/CDs/H-Gel)

Hydrogel was formed by Schiff base-based crosslinking between amine groups of quaternized chitosan and aldehyde groups of oxidized alginates. Moreover, CDs were incorporated into the hydrogel along with UDC drug to prepare UDC/CDs/H-Gel. FT-IR spectroscopy was utilized to confirm the quaternization of amine groups present in chitosan and oxidation of alginate (**Figure S6 and S7**, **Supporting Information**). In the case of QCS, a new peak at 1480 cm^{-1} appeared that was ascribed to asymmetric C–H stretching of methyl groups of quaternary ammonium groups along with all the peaks that were present in chitosan.[42] In the case of OA, a new peak at 1715 cm^{-1} appeared corresponding to carbonyl of aldehyde groups formed after oxidation along with all the peaks that were present in alginate.[42] FT-IR spectrum of UDC displayed the peaks at 3234 cm^{-1}

View Article Online
DOI: 10.1039/D5TB00800J

(O–H stretching), 2928 cm^{-1} (C–H stretching), 1720 cm^{-1} (C=O stretching), and 1378 cm^{-1} (C–O stretching of carboxylic acid group) (**Figure S8**, **Supporting Information**).[12] **Figure 2** displays the comparative FT-IR spectra of QCS, OA, and UDC/CDs/H-Gel. FT-IR spectrum of UDC/CDs/H-Gel displayed the peaks at 3400 cm^{-1} (O–H, N–H stretching), 2926 cm^{-1} (C–H stretching), and 1633 cm^{-1} (C=N stretching). It showed the Schiff base-based crosslinking between amine groups of quaternized chitosan and aldehydic groups of oxidized alginate in the hydrogel layer. Electrostatic interactions and hydrogen bonding may additionally strengthen this Schiff base-based polymeric network established by chitosan and alginate. Here, the carboxyl and hydroxyl functional groups present on the surfaces of CDs and UDC can participate in electrostatic interaction and hydrogen bonding with the amine groups of chitosan and the carboxyl groups of alginate.

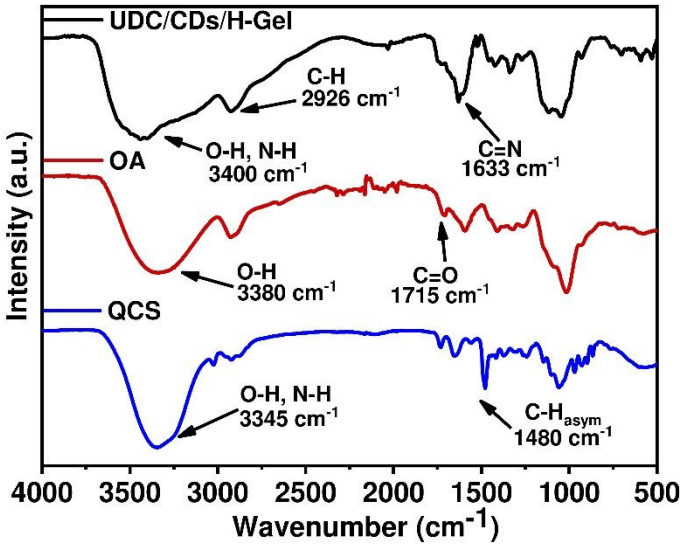

Figure 2. Comparative FT-IR spectra of quaternized chitosan (QCS), oxidized alginate (OA), and UDC/CDs/H-Gel.

Further, XPS analysis of UDC/CDs/H-Gel was also carried out to confirm the chemical composition and Schiff base-based crosslinking in the hydrogel (**Figure S9**, **Supporting Information**). XPS survey spectrum for UDC/CDs/H-Gel is presented in **Figure S9A** in **Supporting Information** showing carbon, oxygen, and nitrogen peaks. High resolution C1s spectrum showed three peaks of O–C=O, C=N, and C–C with binding energy of 288 eV, 286.4 eV, and 284.7 eV, respectively (**Figure S9B**, **Supporting Information**).[47] O1s XPS spectrum consisted of two oxygen peaks (**Figure S9C**, **Supporting Information**). Peak at 532.5 eV was due to O–C bond, and peak at 530.9 eV was consistent with O=C.[47] Moreover, N1s spectrum

View Article Online
DOI: 10.1039/D5TB00800J

presented two peaks upon deconvolution, which were related to $N(CH_3)_3^+$ and N=C with binding energy of 401.8 eV and 399.9 eV, respectively (**Figure S9D**, **Supporting Information**).[47] Fabricated UDC/CDs/H-Gel was also characterized using SEM and the results have been discussed later in **section 3.4**.

3.4. Formation of bilayer dressing (BL)

Bilayer dressing was prepared by using the vacuum filtration method that led to the formation of strong interface between the two layers. Scanning electron microscopic analysis was carried out to examine the morphology of the bilayer dressing both on the surface and at the interface. As reported in the literature, immersion and coating approaches provide weak interfacial adhesion between the two layers, which may cause cracking.[49] On the contrary, in vacuum filtration process, the hydrogel forming solution is able to penetrate the pores of nanofiber layer, which creates strong interfacial adhesion between hydrogel and nanofiber layer.[49] Porous morphology of UDC/CDs/H-Gel layer can be easily seen in **Figure 3A**. Further, elemental mapping of UDC/CDs/H-Gel confirmed that all the elements were evenly distributed across the hydrogel (**Figure S10, Supporting Information**). For comparison, SEM imaging and elemental mapping of H-Gel were also carried out, revealing a porous morphology with a uniform elemental distribution throughout the hydrogel (**Figure S11, Supporting Information**). The morphology of the NF layer shown in **Figure 3B** displayed smooth and uniform surface of electrospun nanofibers, and the average diameter of nanofibers was 228 ± 61 nm (**Figure S12, Supporting Information)**. Structural integrity of bilayer matrix at the interface of hydrogel and NF layer was also observed by SEM (**Figure 3C**).

View Article Online
DOI: 10.1039/D5TB00800J

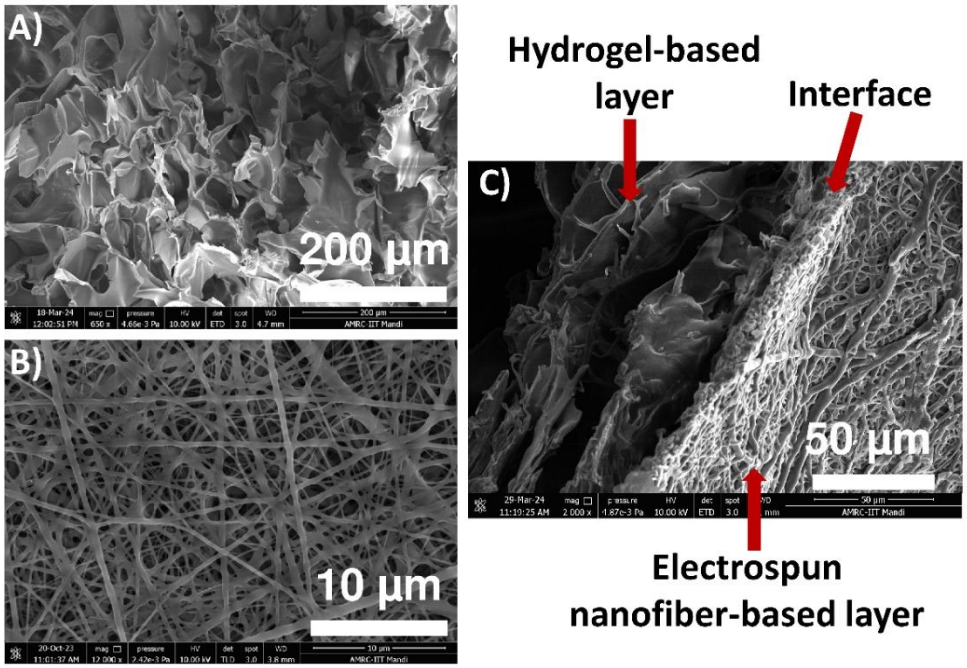

Figure 3. SEM image of bilayer dressing (BL). (A) Bottom UDC/CDs/H-Gel layer of BL. Scale bar: 200 µm. (B) Top NF layer of BL. Scale bar: 10 µm. (C) Interface between UDC/CDs/H-Gel and NF layers in BL. Scale bar: 50 µm.

3.5. Mechanical studies

Tensile strength and elongation at break were assessed to determine the influence of loading of CDs and UDC in hydrogel layer (UDC/CDs/H-Gel). Further, the impact of integrating NF layer with UDC/CDs/H-Gel layer on the mechanical behavior was also evaluated. A comparison for the tensile strength of H-Gel, UDC/CDs/H-Gel, and BL is shown in **Figure 4A**. It was observed that loading of CDs and UDC in UDC/CDs/H-Gel led to a ~34% enhancement in tensile strength as compared to unloaded H-Gel. The enhanced tensile strength can be correlated to the loaded material serving as a reinforcing filler. Additionally, the hydrogen bonding interactions between the carboxyl and hydroxyl groups of CDs and UDC with the amine groups of chitosan, as well as the carboxylic groups of alginate in the hydrogel layer, may further contribute to this enhancement in tensile strength. Similar findings have been reported by Kalaycıoğlu *et al.*[50] Further, integration of NF with UDC/CDs/H-Gel layer led to ~45% increment in tensile strength. This enhancement could be due to the formation of interpenetrating network at the interface of two layers, which was supported by SEM image of BL.[51] Elongation at break of H-gel, UDC/CDs/H-Gel, and BL is shown in **Figure 4B**. A ~17% increment was observed with the loading of CDs and UDC in

View Article Online
DOI: 10.1039/D5TB00800J

UDC/CDs/H-Gel layer as compared to H-Gel. This increment can be attributed to CDs and UDC inhabiting the interchain gaps within the polymer network, thereby expanding the spacing between polymer chains. Comparable results have been reported by Riahi *et al.*[52] Additionally, the integration of nanofibers and hydrogel in BL resulted in a ~48% increment in elongation at break. This increase may result from the entanglement of polymer chains at the interface of two layers, which can improve elongation at break, thereby aiding in withstanding the external forces.[53] For comparison, mechanical strength of NF was measured separately showing tensile strength of 2.57 MPa and elongation at break of 111% (**Figure S13, Supporting Information**).

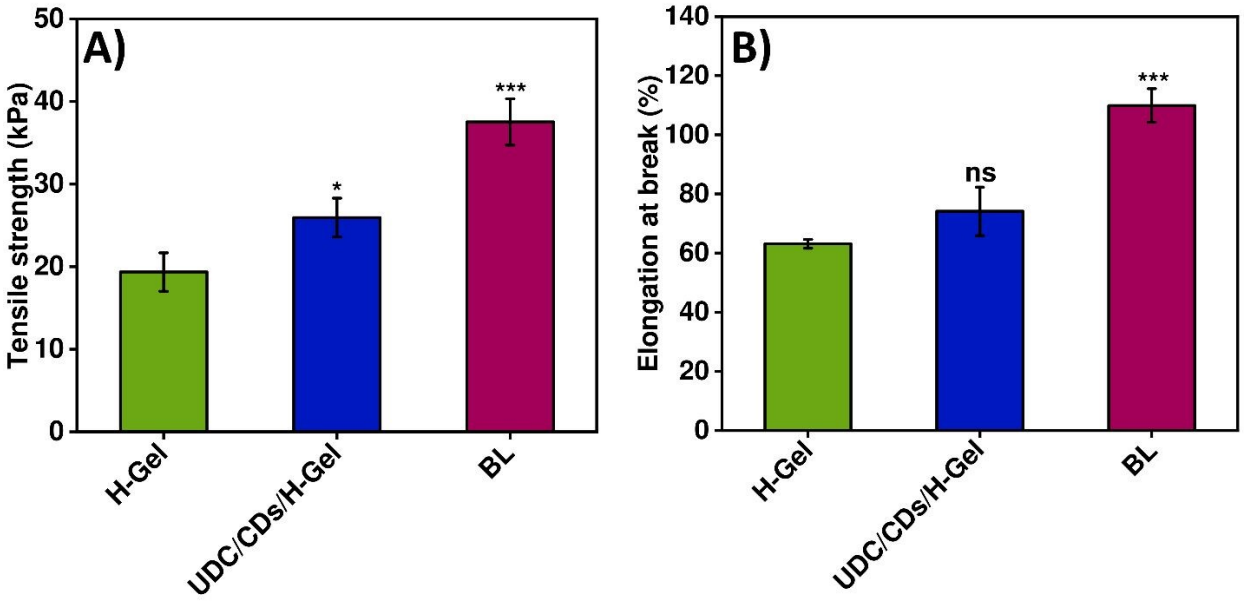

Figure 4. Evaluation of mechanical properties. (A) Tensile strength of H-Gel, UDC/CDs/H-Gel, and BL. (B) Elongation at break of H-Gel, UDC/CDs/H-Gel, and BL. The data are expressed as mean ± standard deviation (n = 3), with significance levels indicated by P values <0.05 (*), 0.01 (**) and 0.001 (***).

3.6. Swelling and degradation studies

Swelling behavior of H-Gel, UDC/CDs/H-Gel, NF, and BL was assessed in buffer solution of pH 7.4 and pH 8.5. These pH values were selected to represent the physiological environment (pH 7.4) and the alkaline conditions often associated with bacteria-infected wounds (pH 8.5).[54] Experimental results showed that H-Gel and UDC/CDs/H-Gel displayed ~200% swelling in buffer solutions over 36 h (**Figure S14, Supporting Information**). With further incubation, hydrogels showed slight degradation. Additionally, the incorporation of CDs and UDC showed no significant

View Article Online
DOI: 10.1039/D5TB00800J

impact on the swelling and degradation properties of the hydrogels. Similarly, NF also showed increase in swelling at both pH 7.4 and pH 8.5 (**Figure S14, Supporting Information**). Initially, up to 12 h, capacity of swelling was higher in the case of NF (~460% swelling) as compared to H-Gel and UDC/CDs/H-Gel. Further, nanofibers showed degradation with increase in incubation time. As displayed in **Figure 5A**, BL showed enhanced swelling behavior (~400% swelling in 36 h) at both pH 7.4 and pH 8.5 as compared to hydrogels. It was observed that BL displayed degradation with increasing incubation time over 100 h.

These results highlight that NF exhibited the highest swelling over 12 h but degraded faster, whereas hydrogels showed the lowest swelling and maintained structural integrity longer than NF. Overall, BL demonstrated intermediate swelling and degradation behavior as compared to its monolayer counterparts.

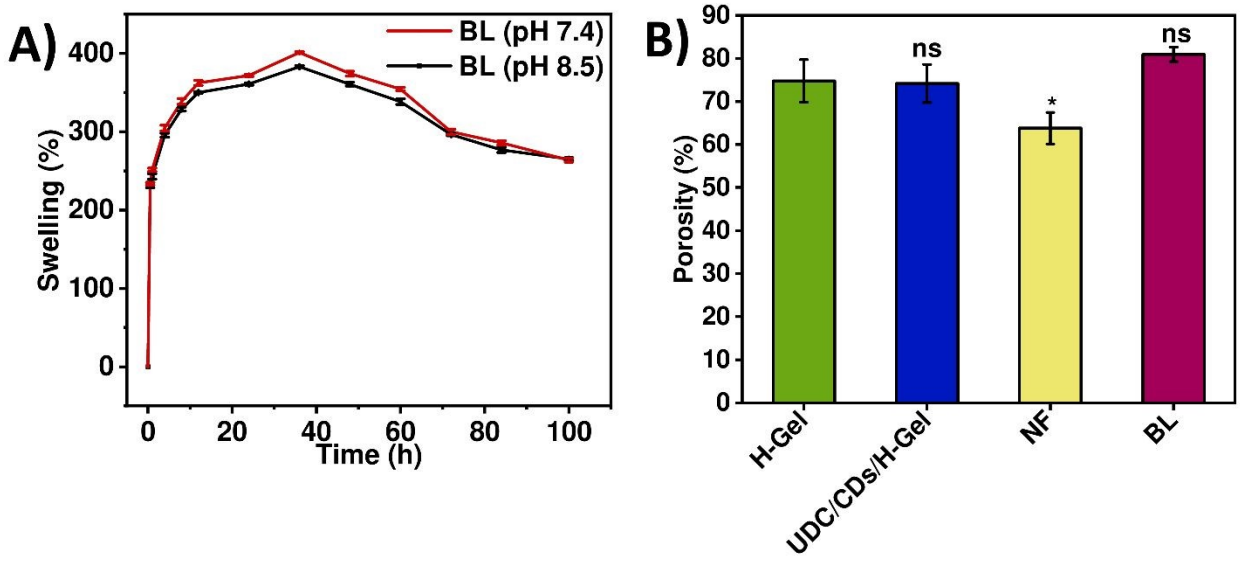

Figure 5. (A) Swelling and degradation behavior of BL at pH 7.4 and pH 8.5. (B) Porosity of H-Gel, UDC/CDs/H-Gel, NF, and BL. The data are expressed as mean ± standard deviation (n = 3), with significance levels indicated by P values <0.05 (*), 0.01 (**) and 0.001 (***).

3.7. Porosity measurements

Ethanol displacement method was utilized to ascertain the porosity of H-Gel, UDC/CDs/H-Gel, NF, and BL as ethanol cannot dissolve the lyophilized form of chitosan, alginate, and gelatin (**Figure 5B**). It was observed that the porosity of UDC/CDs/H-Gel was almost similar to H-Gel suggesting negligible influence of CDs and UDC incorporated in hydrogel layer. In the case of BL, there was slight increase in porosity with no significant difference with respect to hydrogels

View Article Online
DOI: 10.1039/D5TB00800J

(**Figure 5B**). Upon combining nanofiber layer and hydrogel layer together, the interfacial interactions between them can introduce additional voids even if those layers were strongly bonded, as supported by SEM image in **Figure 3**. This architectural complexity may have allowed ethanol, used in ethanol displacement method, to access more voids resulting in a slightly higher total porosity.

3.8. Contact angle measurements

Sessile drop method was employed to measure water contact angle for evaluating surface wettability on both the sides of BL, which influences cell adhesion and overall biocompatibility. The result showed that the water contact angle of UDC/CDs/H-Gel layer side and NF layer side were 63.2° and 58.5°, respectively, thus, confirming the presence of hydrophilic surface on both the sides of BL (**Figure S15, Supporting Information)**. Furthermore, the water contact angle of UDC/CDs/H-Gel layer (58.5°) was lower as compared to unloaded H-Gel (67.3°), which may be attributed to the hydrophilic nature of UDC.

3.9. *In vitro* UDC release from UDC/CDs/H-Gel

UDC is a promising option for wound-healing applications due to its inhibition of NF-κB activation, and its anti-inflammatory and tissue regeneration properties.[55, 38] *In vitro* release of UDC from UDC/CDs/H-Gel (loading efficiency = 10%) was studied at pH 7.4 and pH 8.5 over 100 h, and the samples were collected at regular intervals. The chosen pH values reflect the physiological environment (pH 7.4) and the alkaline conditions often related to bacterial infections in wounds (pH 8.5).[54] The experimental results revealed that in initial 10 h, 58% UDC was released at pH 7.4, while 54% UDC was released at pH 8.5. At the end of 100 h, the cumulative UDC release of 90% and 82% were achieved at pH 7.4 and pH 8.5, respectively (**Figure 6A**). Higher UDC release at pH 7.4 can be ascribed to the increased number of protonated amine groups of chitosan, which in turn may influence the interaction of UDC drug with polymeric matrix of hydrogel.[42]

Release of UDC was further analyzed using different release kinetics models and the highest correlation was observed with Korsmeyer−Peppas model indicating both diffusion and erosion-based release (**Figure S16 and Table S1, Supporting Information**).

View Article Online
DOI: 10.1039/D5TB00800J

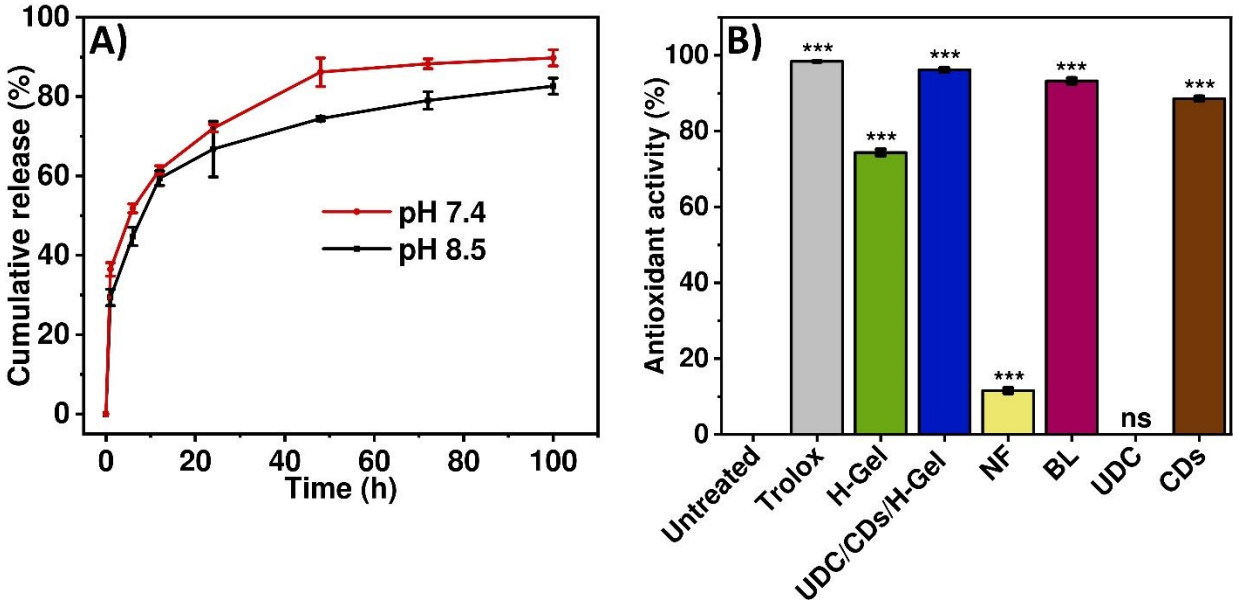

Figure 6. (A) Release profiles of UDC from the UDC/CDs/H-Gel in PBS (pH 7.4 and pH 8.5). (B) Antioxidant activity of H-Gel, UDC/CDs/H-Gel, NF, BL, UDC, and CDs, where untreated DPPH radical solution was used as a negative control and Trolox was used as a positive control. The data are expressed as mean ± standard deviation (n = 3), with significance levels indicated by P values <0.05 (*), 0.01 (**) and 0.001 (***).

3.10. Antioxidant activity

Excessive ROS level may negatively impact the process of wound healing by extending the inflammatory phase.[56] Hence, it is important to eliminate these free radicals in order to foster efficient wound healing. It is notable that CDs present in the hydrogel layer, along with the lone pairs of hydroxyl and amine groups in the polymers, help in shielding cells from oxidative damage.[57]

In this regard, DPPH assay was used to check the antioxidant potential of H-Gel, UDC/CDs/H-Gel, NF, BL, UDC, and CDs by measuring the extent of interaction between sample and purple-colored DPPH radical solution to form stable yellow-colored macromolecular radicals (**Figure 6B**). Around 89% and 74% antioxidant activities were observed for CDs and H-Gel, respectively. The antioxidant activity of UDC/CDs/H-Gel (~96%) increased with the loading of CDs, which is in corroboration with the inherent antioxidant activity of bare CDs. The antioxidant activity of CDs can be primarily attributed to their functional groups (such as –OH, –COOH, –NH_2).[58] Moreover, electron density on the carbon dot surface also helps in increasing antioxidant

View Article Online
DOI: 10.1039/D5TB00800J

activity. As reported in the literature, from the mechanism perspective, this involves hydrogen atom transfer (HAT) and/or single electron transfer (SET) processes.[58] These features synergistically/additively contribute to efficient neutralization of radicals such as DPPH$^{\bullet}$.[58] Further, the integration of NF with UDC/CDs/H-Gel showed no discernible difference in antioxidant activity of BL (~93%).

3.11. Antibacterial activity

A quantitative assessment of antibacterial activity was done using the optical density (OD_{600}) method to evaluate the effect of H-Gel, UDC/CDs/H-Gel, NF, BL, UDC, and CDs against *S. aureus* and *E. coli* (**Figure 7A and B**). It is to be noted that H-Gel by itself showed 58% and 60% antibacterial activity against *E. coli* and *S. aureus*, respectively. This intrinsic antibacterial behavior can be attributed to the interaction of positively charged quaternary amine group of quaternized chitosan with negatively charged phosphatidylglycerol moieties residing in bacterial membranes.[59] Further, UDC/CDs/H-Gel showed 81% and 69% antibacterial activity against *E. coli* and *S. aureus* respectively. The enhanced efficacy of UDC/CDs/H-Gel can be ascribed to the additive effect of positively charged quaternized chitosan and CDs incorporated inside the film. The antibacterial activity of CDs can be ascribed to its interaction with the bacterial cell walls, leading to the distortion of bacterial membrane.[60] On the other hand, NF showed 41% and 51% antibacterial activity against *E. coli* and *S. aureus,* respectively owing to the presence of amine groups present in gelatin and chitosan. Furthermore, the integration of both hydrogel and NF layers in BL led to a substantial increase in its antibacterial activity. BL showed 92% and 88% antibacterial activity against *E. coli* and *S. aureus* respectively, within 24 h.

Antibacterial behavior of BL was further supported by live-dead staining of *S. aureus* and *E. coli* (**Figure 7Cand D**). SYTO 9 and propidium iodide (PI) were used to stain bacterial cells that had been treated with BL for 24 h. PI preferably combines with the DNA of cells exhibiting compromised membrane integrity and emits red fluorescence. In cells with intact membranes, SYTO 9 interacts with both DNA and RNA, resulting in green fluorescence, which indicates viable cells. The experimental results showed that untreated bacterial cells displayed green fluorescence confirming live cells, whereas bacterial cells treated with the BL exhibited red fluorescence. Here, the decrease in green fluorescence and the increase in red fluorescence indicated significantly higher percentage of dead cells in BL-treated bacteria as compared to control sample consisting of untreated bacteria.

View Article Online
DOI: 10.1039/D5TB00800J

Further, TEM analysis (**Figure 7E and F**) was employed to examine the antibacterial mechanism of BL against both *S. aureus* and *E. coli*. Here, untreated bacterial cells maintained their structural integrity, with cell membrane remaining intact. Conversely, BL treatment caused evident disruptions in the bacterial cell membranes, leading to the leakage of cytoplasmic content and finally resulting in cell death.

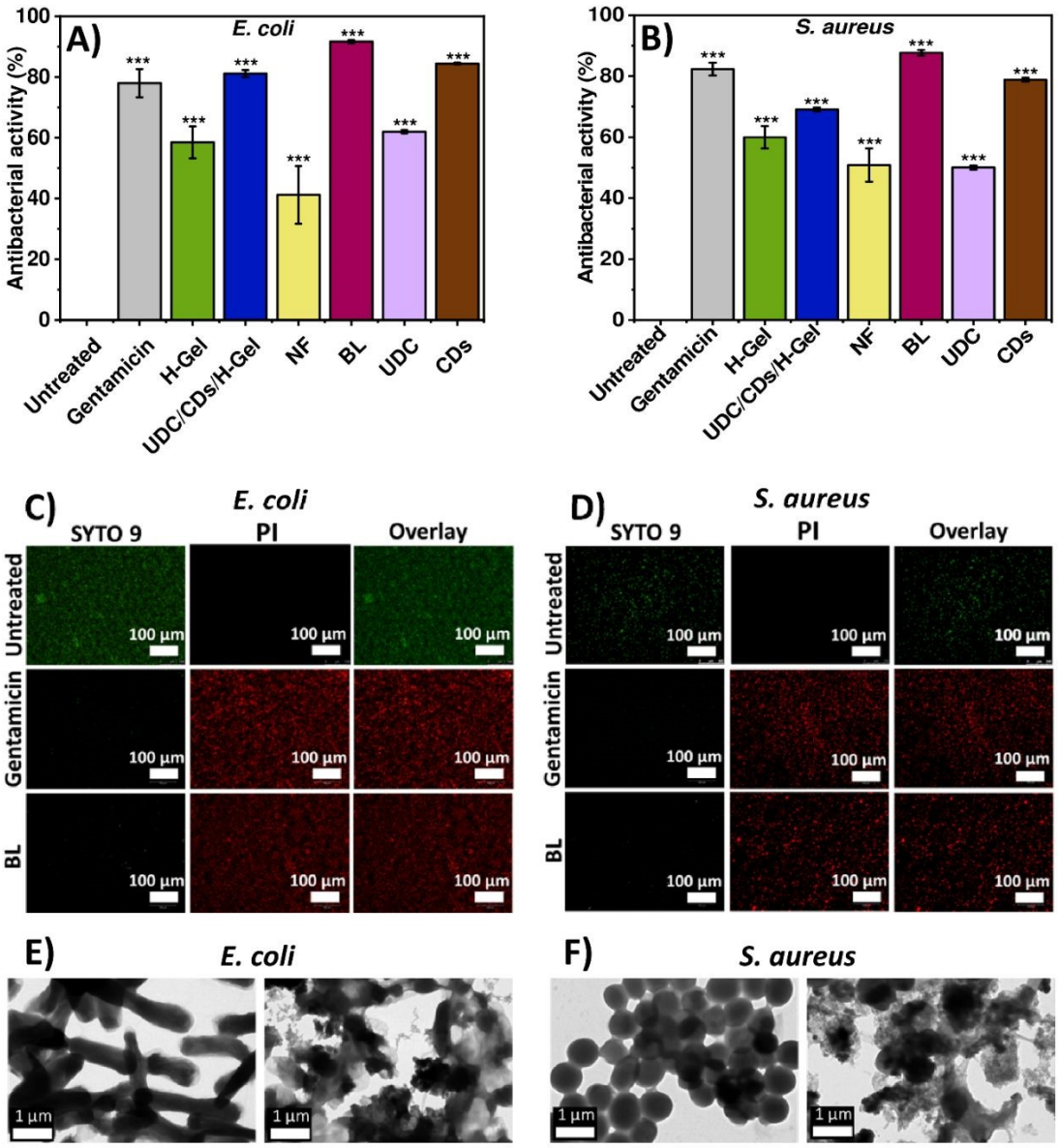

Figure 7. Antibacterial activity of H-Gel, UDC/CDs/H-Gel, NF, BL, UDC, and CDs against (A) *E. coli*, and (B) *S. aureus*. Live-Dead assay of (C) *E. coli*, and (D) *S. aureus*. Scale bar: 100 µm. Here, untreated bacteria were used as a negative control and gentamicin sulphate-treated bacteria

View Article Online
DOI: 10.1039/D5TB00800J

were used as a positive control. TEM analysis to examine the antibacterial mechanism: (E) untreated *E. coli* and *E. coli* treated with BL, and (F) untreated *S. aureus* and *S. aureus* treated with BL. Scale bar: 1 µm. The data are expressed as mean ± standard deviation (n = 3), with significance levels indicated by P values <0.05 (*), 0.01 (**) and 0.001 (***).

3.12. Cell viability studies

MTT assay was utilized to compare the viability of murine fibroblast cells (L929) after treatment with H-Gel, UDC/CDs/H-Gel, NF, BL, UDC, and CDs (**Figure 8**). It was observed that H-Gel, UDC/CDs/H-Gel, and NF exhibited cell viability of ~102%, ~97%, and ~108%, respectively, whereas UDC and CDs showed cell viability of ~140% and ~43%, respectively. Further, BL demonstrated a significantly enhanced cell viability of ~130%, surpassing the individual monolayer counterparts. It is to be noted that in addition to similar cell viability as UDC, BL also offers additional benefits, such as antioxidant and antibacterial activity, which is useful for effective wound healing.

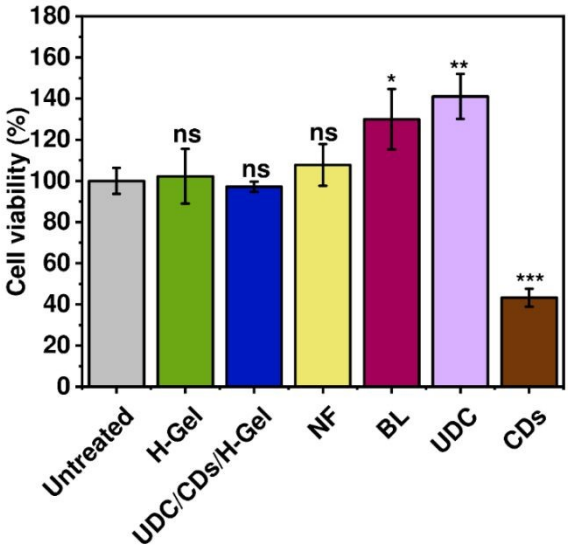

Figure 8. Cell viability studies of murine fibroblasts (L929) cells treated with H-Gel, UDC/CDs/H-Gel, NF, BL, UDC, and CDs, where untreated cells were utilized as a control. The data are expressed as mean ± standard deviation (n = 3), with significance levels indicated by P values <0.05 (*), 0.01 (**) and 0.001 (***).

Moreover, live-dead assay was carried out to compare the cytocompatibility of H-Gel, UDC/CDs/H-Gel, NF, BL, UDC, and CDs (**Figure 9**). Untreated cells were utilized as a control. Here, ethidium homodimer-1 and calcein AM were used together for cell staining. Ethidium

View Article Online
DOI: 10.1039/D5TB00800J

homodimer-1 selectively binds to dead cells, producing a red fluorescence, while calcein AM permeates live cells and emits green fluorescence, indicating cell viability. It was observed that in the case of UDC drug, the density of live cells was the highest. On the other hand, in the case of CDs, fraction of dead cells was the highest as compared to other test groups owing to the dose dependent cytotoxicity as evidenced by results reported by Zhang *et al*.[40] It was observed that H-Gel, UDC/CDs/H-Gel, and NF showed good cell viability. However, UDC/CDs/H-Gel also showed the presence of a few dead cells as compared to H-Gel, which may be attributed to the presence of CDs. Notably, BL showed excellent cell viability, as confirmed by a high density of live cells and no visible dead cells. Additionally, BL mitigates the impact of CDs, thus, ensuring a favorable environment for enhanced cell viability and proliferation as compared to its monolayer counterparts. The exact mechanism by which BL accomplishes increase in cell viability is not yet clear, but it may be related to physical obstructions within the system.[61] This further supported the MTT assay results and validated the cytocompatibility and cell proliferating nature of BL.

In addition to the extract-based cytocompatibility assessment, direct cell culture studies on the both sides of BL were also carried out. This experiment confirmed that, after 24 h, both surfaces supported cell adhesion, indicating the material's suitability for direct cell-material interaction (**Figure S17, Supporting Information**). Notably, the NF showed relatively higher cell adhesion as compared to the UDC/CDs/H-Gel. NF offers a robust structure that promotes efficient cell adhesion and the presence of gelatin matrix concurrently provides a bioactive environment that promotes cell adhesion. Similar results have been reported by Ramanathan *et al*.[35]

View Article Online
DOI: 10.1039/D5TB00800J

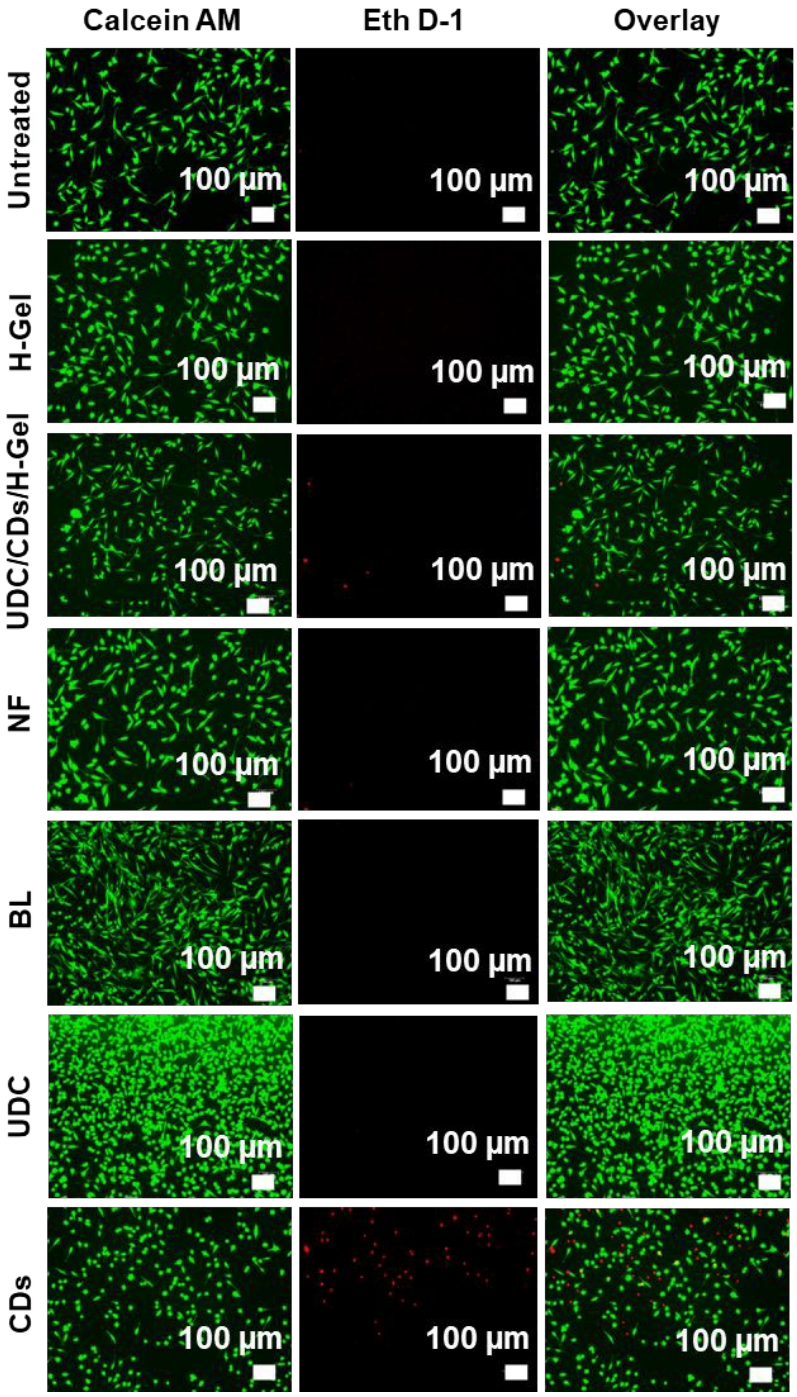

Figure 9. Live-dead images of murine fibroblasts (L929) cells treated with H-Gel, UDC/CDs/H-Gel, NF, BL, UDC, and CDs, where untreated cells were utilized as a control. Scale bar: 100 µm.

3.13. ROS scavenging studies

H_2DCFDA assay was carried out to examine the ROS scavenging ability of H-Gel, UDC/CDs/H-Gel, NF, BL, UDC, and CDs in H_2O_2-treated L929 cells (**Figure 10**). Cell-permeable H_2DCFDA

View Article Online
DOI: 10.1039/D5TB00800J

undergoes deacetylation by cellular esterases, resulting in the formation of 2′,7′-dichlorodihydrofluorescein. Upon exposure to ROS, it is rapidly oxidized into highly fluorescent 2′,7′-dichlorofluorescein.[57] To assess ROS scavenging ability of the test samples, cells were first exposed to H_2O_2 to induce ROS generation. Subsequently, these ROS induced cells were treated with desired samples. Here, untreated cells (without any exposure to H_2O_2) were used as a control, which showed a fluorescence intensity of ~2000. The H_2O_2-treated cells showed a significantly higher fluorescence intensity of ~13412, thus, confirming the substantial ROS generation. The experimental results showed that H-Gel treated cells exhibited fluorescence intensity of ~4000 indicating substantial ROS scavenging. This can be ascribed to the presence of quaternized chitosan in hydrogel matrix that caused significant increase in the capability of ROS neutralization, which is notably higher than pure chitosan.[62, 63]

UDC/CDs/H-Gel-treated cells showed improved ROS scavenging ability, lowering the fluorescence intensity further to ~3000, which can be correlated to the antioxidant activity of CDs. In contrast, NF-treated cells showed increase in fluorescence intensity (~11000), thus, showing poor ROS scavenging behavior. Although chitosan present in NF contains amine groups that can interact with ROS, their scavenging ability may not be sufficient to effectively neutralize ROS. Similar observations have been reported by Wu *et al.*[64] Among the test samples, UDC-treated cells displayed the highest fluorescence intensity (~12000), demonstrating its minimal scavenging potential, whereas CDs treated cells showed relatively better ROS scavenging ability with a fluorescence intensity of ~3500. Notably, BL-treated cells showed a discernible decrease in fluorescence intensity (~2400), which is very close to the control and significantly lower than H_2O_2-treated cells. This highlights the excellent ROS scavenging ability of BL and the obtained findings are in accordance with the antioxidant studies conducted employing DPPH assay.

View Article Online
DOI: 10.1039/D5TB00800J

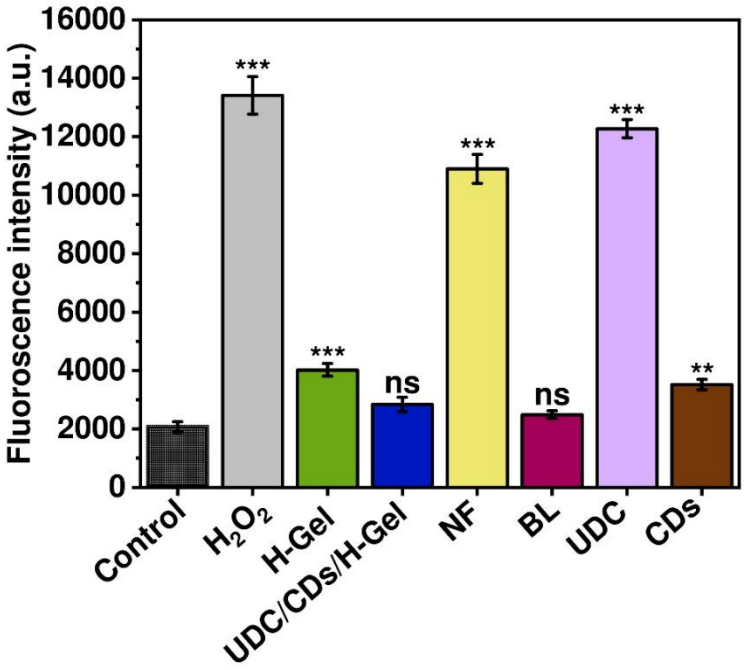

Figure 10. ROS scavenging analysis of H-Gel, UDC/CDs/H-Gel, NF, BL, UDC, and CDs in H_2O_2-treated murine fibroblasts (L929) cells, where untreated cells were utilized as a control. The data are expressed as mean ± standard deviation (n = 3), with significance levels indicated by P values <0.05 (*), 0.01 (**) and 0.001 (***).

3.14. Hemolysis assay

RBCs are indicative of the body's overall response to the treatment.[65] Hence, hemocompatibility of H-Gel, UDC/CDs/H-Gel, NF, BL, UDC, and CDs were assessed using hemolysis assay. The experimental results indicated that the test samples caused minimal disruption to RBCs. Here, CDs showed maximum hemolysis of ~6% and BL showed minimum hemolysis (~4.5%), whereas triton-X (positive control) treated RBCs resulted in crimson color solution attributed to the complete lysis of RBCs (**Figure S18, Supporting Information**). The percentage of hemolysis for BL was less than 5%, adhering to the acceptable threshold for biomaterials.[4]

3.15. Hemostatic activity

To evaluate the hemostatic potential of H-Gel, UDC/CDs/H-Gel, NF, BL, UDC, and CDs, whole blood clotting test was performed considering untreated blood as a control. It involves measuring the absorbance of hemoglobin in uncoagulated blood. The reduced absorbance of hemoglobin signifies increased immobilization of RBCs by the material, consequently leading to enhanced clot formation.[42] It was observed that among all the test groups, BL and UDC/CDs/H-Gel showed

View Article Online
DOI: 10.1039/D5TB00800J

maximum reduction in hemoglobin absorbance value in comparison to untreated blood that may be attributed to the additive effect of polymer matrix, UDC, and CDs. (**Figure S19, Supporting Information**). The results obtained in our study are comparable to reported literature by Xia *et al.*[4]

3.16. Scratch assay

Scratch assay was performed to examine the *in vitro* wound healing capability of BL and its monolayer counterparts (**Figure 11A**). In this regard, a scratch was made on monolayer of cells followed by incubation with test samples. Untreated cells were utilized as a control here. To monitor the healing, images were taken at 0, 12, and 24 h using a microscope. Quantitative analysis of the scratch area using ImageJ software revealed the wound closure capability of different test samples (**Figure 11B**). After 24 h, ~49% unhealed scratch area was noted in the case of untreated cells. Among the tested monolayer counterparts, UDC/CDs/H-Gel showed the highest wound closure efficiency, with ~24% unhealed scratch area after 24 h. On the other hand, NF and H-Gel showed similar levels of healing with ~40% unhealed scratch area after 24 h. Interestingly, scratch treated with BL exhibited a faster wound closure with only ~3% unhealed scratch area after 24 h. This clearly indicates the enhanced effectiveness of BL for wound healing by significantly outperforming both the untreated group and the monolayer counterparts.

A comparative analysis of the current study with previously reported studies in the literature is shown in **Table 1.**

View Article Online
DOI: 10.1039/D5TB00800J

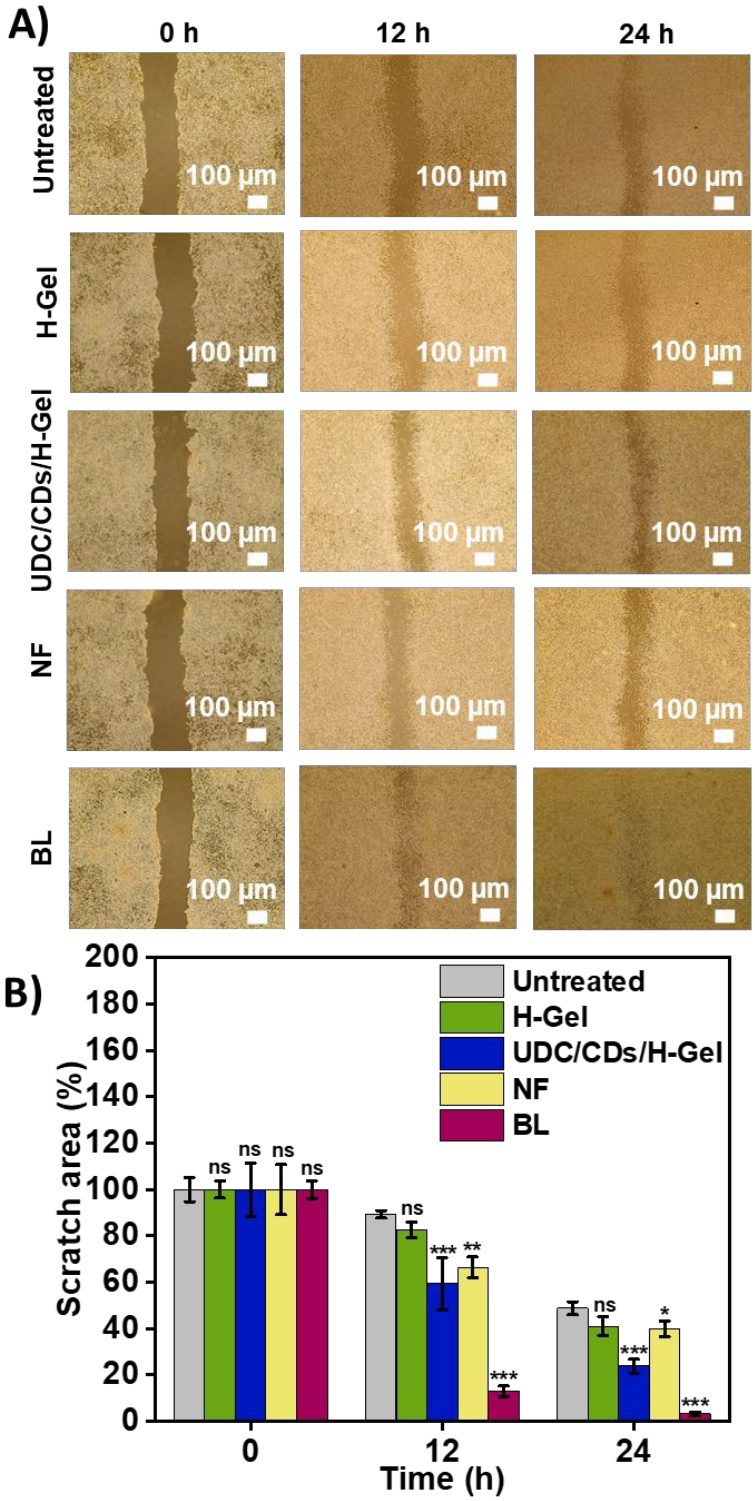

Figure 11. *In vitro* wound healing using murine fibroblasts (L929) cells. (A) Scratch images in the case of H-Gel, UDC/CDs/H-Gel, NF, and BL for 0, 12, and 24 h. Scale bar: 100 µm. (B) Quantitative estimation of the wound closure in the cases of NF, H-Gel, UDC/CDs/H-Gel, and BL. Here, untreated cells were utilized as a control. The data are expressed as mean ± standard

View Article Online
DOI: 10.1039/D5TB00800J

deviation (n = 3), with significance levels indicated by P values <0.05 (*), 0.01 (**) and 0.001 (***).

544

Table 1. Comparative analysis of different wound healing matrices reported in the literature with the current study.

S. No.	System	Antioxidant activity	Antibacterial activity	Cell viability	ROS scavenging ability	Hemostatic behavior	*In-vitro* wound closure	Ref.
1.	Oxytetracycline loaded lignin/chitosan/polyvinyl alcohol-based hydrogel	39.27%	ZOI: 22 mm for *E. coli* and 24.5 mm for *S. aureus*	~85% (L929)	-	-	7.2% cell migration in 4 h (L929)	Preet *et al.*[66]
2.	Glucose oxidase and catalase nanoenzyme–chitosan hydrogel	-	OD_{600}: ~78% for *E. coli* and ~95% for *S. aureus*	~110% (L929 and HUVECs)	Yes	-	38.37% (L929) and 74.12% (HUVECs) cell migration in 24 h	Li *et al.*[67]
3.	Carboxymethyl chitosan/tannic acid/Cu^{2+} based hydrogel	-	CCM: 100% for methicillin-resistant *S. aureus* death in 12 days	~90% (HEK and HUVECs)	-	-	~95% wound closure (HEK) after 6 h	Lin *et al.*[68]
4.	Photocatalytic graphene nanocomposite and curcumin loaded chitosan/polyvinyl alcohol-based hydrogel	-	ZOI: 18 mm for *E. coli*, 17 mm for *P. aeruginosa*, 16 mm for *S. aureus*, and 15 mm for *E. faecalis*	~98% (NIH3T3)	-	Yes	~99% wound closure (NIH3T3) after 48 h	Jayabal *et al.*[69]

5.	Poly glycerol sebacate/poly lactide acid/platelet-rich plasma electrospun nanofibers	-	-	~100% (L929, HUVEC, and RAW-264.7)	-	-	~99% wound closure (L929) after 24 h	Heydari *et al.*[70]
6.	BL	□93%	OD_{600}: 92% for *E. coli* and 88% for *S. aureus*	~130% (L929)	Yes	Yes	~97% wound closure	Current study

ZOI: Zone of inhibition; CCM: Colony counting method.

View Article Online
DOI: 10.1039/D5TB00800J

4. Conclusions

Herein, bilayer dressing (BL) was developed, which mimics the dermal and epidermal architecture of normal skin by integrating electrospun nanofiber-based layer (NF) with hydrogel layer loaded with ursodeoxycholic drug (UDC) and carbon dots (CDs). BL was imparted with multiple active features like antioxidant, antibacterial, hemostasis, and reactive oxygen species (ROS) scavenging ability for enhanced wound healing. BL exhibited remarkable swelling behavior and porosity as compared to hydrogel layer. Additionally, the integration of nanofiber-based layer with hydrogel layer in BL led to a significant enhancement in the tensile strength and elongation at break, thereby, demonstrating its improved mechanical behavior. BL showed excellent antioxidant activity (~93%) and antibacterial activities against *E. coli* (92%) and *S. aureus* (88%). Cell viability studies, including MTT and Live-dead assay, demonstrated enhanced cell viability in the case of BL as compared to individual NF and hydrogel layer. Further, BL outperformed its monolayer counterparts by displaying excellent hemocompatibility and enhanced wound closure, thus opening a new pathway for the healing of infectious wounds.

Author information

Corresponding author

Garima Agrawal – School of Chemical Sciences and Advanced Materials Research Centre, Indian Institute of Technology Mandi, Mandi-175075, Himachal Pradesh, India

ORCID: https://orcid.org/0000-0002-3391-2378

E-mail: garima@iitmandi.ac.in

Authors

Dimpy Bhardwaj – School of Chemical Sciences and Advanced Materials Research Centre, Indian Institute of Technology Mandi, Mandi-175075, Himachal Pradesh, India

ORCID: https://orcid.org/0009-0009-9115-2555

Vatan Chawla – Department of Chemistry, Indian Institute of Technology Ropar, Rupnagar-140001, Punjab, India

Vanshika Nandwani – School of Chemical Sciences and Advanced Materials Research Centre, Indian Institute of Technology Mandi, Mandi-175075, Himachal Pradesh, India

View Article Online
DOI: 10.1039/D5TB00800J

Yashika Thakur – Department of Chemistry, Indian Institute of Technology Ropar, Rupnagar-140001, Punjab, India

Yashveer Singh – Department of Chemistry, Indian Institute of Technology Ropar, Rupnagar-140001, Punjab, India

ORCID: https://orcid.org/0000-0003-1625-8156

Author contributions

D.B.: Data curation and analysis, writing an initial version of the manuscript, and figure preparation; V.C.: Data curation for biological studies; V.N.: Data curation; Y.T.: Data curation; Y.S.: Supervision of biological studies and editing of manuscript; G.A.: Conceptualization, supervision, and manuscript preparation.

Data availability

Data available within the article or its supporting information.

Conflicts of interest

The authors declare no conflict of interest.

Acknowledgements

GA thanks the financial support from ANRF Science & Engineering Research Board (SERB-ANRF), India (Grant No. WEA/2023/000001). VC is thankful to the Ministry of Education for the Prime Minister Research Fellowship (PMRF, Application No. PMRF-192002-167) and YS is thankful to DST/GITA India-Taiwan S&T Cooperation Program – Call for Proposal 2021 (grant # GITA/DST/TWN/P-98/2022 for the financial assistance.

References

1. Y. Cheng, X. Liu, F. Fan, Y. Zhang, M. Cao, L. Bai, H. Ming, H. Chen, Y. Liu and Y. Yu, *Biomater. Sci.*, 2025, **13**, 758-776.
2. Q. Lu, X. Tang, B. Tao, K. Huang, K. Li, C. Liu, B. Gao, M. Xu, W. Geng, K. Li and F. Zhou, *Int. J. Biol. Macromol.*, 2025, **296**, 139685.
3. Y. Wang, C. Chen, C. He, W. Dong, X. Yang, Q. Kong, B. Yan and J. He, *Carbohydr. Polym.*, 2025, **348**, 122865.

View Article Online
DOI: 10.1039/D5TB00800J

4. Y. Xia, S. Yan, H. Wei, H. Zhang, K. Hou, G. Chen, R. Cao and M. Zhu, *ACS Appl. Mater. Interfaces*, 2024, **16**, 34578-34590.
5. A. Sood, M. S. Granick and N. L. Tomaselli, *Adv. Wound Care*, 2013, **3**, 511-529.
6. G. D. Winter, *Nature*, 1962, **193**, 293-294.
7. Y. Liang, J. He and B. Guo, *ACS Nano*, 2021, **15**, 12687-12722.
8. X. Zhang, Y. Liang, S. Huang and B. Guo, *Adv. Colloid Interface Sci.*, 2024, **332**, 103267.
9. C. Cheng, R. Wang, J. Ma, Y. Zhang, Q. Jing and W. Lu, *Int. J. Biol. Macromol.*, 2024, **267**, 131237.
10. A. Bužarovska, J. P. Stanoeva, P. Karamanolevski, A. D. Popa, S. Dinescu and L. Avérous, *J. Appl. Polym. Sci.*, 2025, **142**, e56708.
11. D. Jafari, M. Gholipourmalekabadi, S. Alizadeh, M. Rajabi Fomeshi, M. Amoupour and A. Samadikuchaksaraei, *Artif. Organs*, 2024, **48**, 117-129.
12. D. Bhardwaj, R. Bhaskar, A. K. Sharma, M. Garg, S. S. Han and G. Agrawal, *ACS Appl. Bio Mater.*, 2024, **7**, 879-891.
13. H. Zhang, X. Lin, X. Cao, Y. Wang, J. Wang and Y. Zhao, *Bioact. Mater.*, 2024, **33**, 355-376.
14. J. Li, Y. Li, C. Guo and X. Wu, *Chem. Eng. J.*, 2024, **481**, 148458.
15. H. S. Zayed, S. Saleh, A. E. Omar, A. K. Saleh, A. Salama and E. Tolba, *Int. J. Biol. Macromol.*, 2024, **261**, 129665.
16. C. Hong, H. Chung, G. Lee, D. Kim, Z. Jiang, S.-H. Kim and K. Lee, *Biomacromolecules*, 2024, **25**, 4344-4357.
17. T. Long, T. Xu, R. Li, Z. Xu, D. Li, C. Mu, L. Yuan and Y. Mu, *Int. J. Biol. Macromol.*, 2024, **254**, 127918.
18. Y. W. Ding, Z. W. Zhang, X. Y. Cui, R. Y. Hu, Y. Li, S. D. Huang, S. Q. Du, J. W. Dao, D. X. Wei, *Chem. Eng. J.*, 2025, **503**, 158387.
19. Y. Li, Y. Wang, Y. Ding, X. Fan, L. Ye, Q. Pan, B. Zhang, P. Li., K. Luo, B. Hu, B. He, Y. Pu, *ACS Nano*, 2024, **18**, 17251-17266.
20. W. Luo, Z. Li, J. Che, X. Li, H. Zhang, J. Tian, C. Wang, G. Y. Li, L. Jin, *ACS Appl. Mater. Interfaces*, 2024, **16**, 34720-34731.
21. A. Martorana, M. Lenzuni, M. Contardi, F. S. S. Palumbo, S. Cataldo, A. Pettignano, V. Catania, D. Schillaci, M. Summa, A. Athanassiou, C. Fiorica, R. Bertorelli, G. Pitarresi, *ACS Appl. Mater. Interfaces*, 2024, **16**, 20186-20201.
22. H. Jiang, L. Li, Z. Li, X. Chu, *Biomed Microdevices*, 2024, **26**, 12.
23. M. W. Pletts, R. E. Burrell, *Wound Repair Regen.*, 2025, **33**, e13249.
24. S. A. Althawab, T. Alsulami, H. Alzahrani and A. Alzahrani, *Colloids Surf. A: Physicochem. Eng. Asp.*, 2024, **698**, 134554.
25. R. Chandrasekaran, U. Ushani, G. Sankar, J. Joseph, K. Natarajan, S. Palani, P. Sridhar, R. Nagaraj and S. Sagadevan, *BionanoScience*, 2025, **15**, 1-21.
26. S. Zaffar, S. Saha, T. Agrawal, S. K. Gupta, P. Gulati, D. Paul, A. Verma, S. Pal, T. Rakshit, *ACS Biomater. Sci. Eng.*, 2025, **11**, 4219-4230.
27. L. Qu, S. Zhao, Q. Chang, Y. Xie, J. Wang, X. Deng, *ACS Appl. Nano Mater.*, 2025, **8**, 9044-9054.
28. L. Li, Y. Wang, S. Hu, X. Chang, Q. Ding, K. Wang, Y. Chen, J. Zheng, *Acta Biomater.*, 2025, **195**, 467-478.
29. M. Rahmati, J. J. Blaker, S. P. Lyngstadaas, J. F. Mano and H. J. Haugen, *Mater. Today Adv.*, 2020, **5**, 100051.

View Article Online
DOI: 10.1039/D5TB00800J

30. M. Mirhaj, M. Tavakoli, J. Varshosaz, S. Labbaf, S. Salehi, A. Talebi, N. Kazemi, V. Haghighi and M. Alizadeh, *Carbohydr. Polym.*, 2022, **292**, 119648.
31. W. Cao, D. Xia, L. Zhou, Y. Liu, D. Wang, C. Lianga and M. Chen, *Mater. Today Phys.*, 2024, **40**, 101316.
32. M. Tavakoli, M. Mirhaj, J. Varshosaz, M. H. Al-Musawi, Y. Q. Almajidi, A. M. Danesh Pajooh, M. Shahriari-Khalaji, F. Sharifianjazi, M. Alizadeh and S. Labbaf, *ACS Appl. Mater. Interfaces*, 2023, **15**, 55276-55286.
33. M. Zhang, S. Gong, K. Hakobyan, Z. Gao, Z. Shao, S. Peng, S. Wu, X. Hao, Z. Jiang and E. H. Wong, *Adv. Sci.*, 2024, **11**, 2309006.
34. B. Lombardi, C. Casale, G. Imparato, F. Urciuolo and P. A. Netti, *Adv. healthc. mater.*, 2017, **6**, 1601422.
35. G. Ramanathan, L. S. Seleenmary Sobhanadhas, G. F. Sekar Jeyakumar, V. Devi, U. T. Sivagnanam and P. Fardim, *Biomacromolecules*, 2020, **21**, 2512-2524.
36. N. Chundayil Kalathil, M. R. Shah, V. C. Lailakumari, P. Prabhakaran, H. Kumarapilla and G. S. V. Kumar, *ACS Appl. Bio Mater.*, 2024, **7**, 6492-6505.
37. A. Eskandarinia, M. Gharakhloo, P. K. Kermani, S. Navid, M. A. Salami, D. Khodabakhshi and A. Samadi, *Carbohydr. Polym.*, 2023, **319**, 121171.
38. P. Li, Z. Chen, K. Meng, Y. Chen, J. Xu, X. Xiang, X. Wu, Z. Huang, R. Lai, P. Li, Z. Lai, X. Ao, Z. Liu, K. Yang, X. Bai and Z. Zhang, *Orthop. Surg.*, 2024, **16**, 183-195.
39. S. M. Galal, S. M. El Kiki, E. M. Elgazzar, *Cell Biochem. Funct.*, 2024, **42**, e70024.
40. Y. Zhang, Z. Li, L. Sheng and A. Meng, *Colloids Surf. A: Physicochem. Eng. Asp.*, 2023, **657**, 130580.
41. J. Sun, W. Jia, J. Guo, N. K. Khanzada, P. Jin, P. W. Wong, X. Zhang and A. K. An, *Desalination*, 2022, **533**, 115742.
42. D. Negi and Y. Singh, *ACS Appl. Nano Mater.*, 2023, **6**, 13616-13628.
43. A. Dhiman, A. K. Sharma, D. Bhardwaj and G. Agrawal, *Int. J. Biol. Macromol.*, 2023, **228**, 323-332.
44. A. Sood, A. Gupta, R. Bharadwaj, P. Ranganath, N. Silverman and G. Agrawal, *Carbohydr. Polym.*, 2022, **294**, 119833.
45. K. Fukada, T. Tajima, M. Seyama, *ACS Appl. Mater. Interfaces*, 2021, **13**, 59006-59011.
46. N. Vladislavić, I. Š. Rončević, M. Buzuk, M. Buljac and I. Drventić, *J. Solid State Electrochem.*, 2021, **25**, 841-857.
47. M. Kehrer, J. Duchoslav, A. Hinterreiter, M. Cobet, A. Mehic, T. Stehrer and D. Stifter, *Plasma Process. Polym.*, 2019, **16**, 1800160.
48. B. B. Campos, C. Abellán, M. Zougagh, J. Jimenez-Jimenez, E. Rodríguez-Castellón, J. C. G. Esteves da Silva, A. Ríos and M. Algarra, *J. Colloid Interface Sci.*, 2015, **458**, 209-216.
49. M. Zhang, S. Xu, C. Du, R. Wang, C. Han, Y. Che, W. Feng, C. Wang, S. Gao, W. Zhao, *Colloids Surf B Biointerfaces*, 2023, **222**, 113119.
50. Z. Kalaycıoğlu, E. Torlak, G. Akın-Evingür, İ. Özen and F. B. Erim, *Int. J. Biol. Macromol.*, 2017, **101**, 882-888.
51. X. He, S. Wang, J. Zhou, D. Zhang, Y. Xue, X. Yang, L. Che, D. Li, S. Xiao and S. Liu, *ACS Appl. Mater. Interfaces*, 2022, **14**, 4579-4587.
52. Z. Riahi, A. Khan, J.-W. Rhim, G. H. Shin and J. T. Kim, *Int. J. Biol. Macromol.*, 2024, **258**, 129302.
53. J. Liu, P. Miao, W. Zhang, G. Song, J. Feng, X. Leng and Y. Li, *Polymer*, 2022, **256**, 125254.

View Article Online
DOI: 10.1039/D5TB00800J

54. H. Haidari, K. Vasilev, A. J. Cowin and Z. Kopecki, *ACS Appl. Mater. Interfaces*, 2022, **14**, 51744-51762.
55. T. Milivojac, M. Grabež, A. Krivokuća, U. Maličević, M. Gajić Bojić, Đ. Đukanović, S. Uletilović, N. Mandić-Kovačević, T. Cvjetković, M. Barudžija, N. Vojinović, A. Šmitran, L. Amidžić, M. P. Stojiljković, M. Čolić, M. Mikov and R. Škrbić, *Mol. Cell. Biochem.*, 2025, **480**, 563-576.
56. C. Huang, Z. Zhang, Y. Fang, K. Huang, Y. Zhao, H. Huang and J. Wu, *Int. J. Biol. Macromol.*, 2024, **278**, 134496.
57. V. Chawla, S. Sharma and Y. Singh, *ACS Biomater. Sci. Eng.*, 2023, **9**, 2647-2662.
58. N. Sharma, A. Sharma, H. J. Lee, *Environ. Chem. Lett.*, 2025, **23**, 1061-1109.
59. Y. Gong, H. Wang and J. Sun, *Biomacromolecules*, 2024, **25**, 4619-4638.
60. J. Hua, P. Hua and K. Qin, *Colloids Surf. A: Physicochem. Eng. Asp.*, 2024, **680**, 132672.
61. T. Wang, Y. Li, Y. Liu, Z. Xu, M. Wen, L. Zhang, Y. Xue and L. Shang, *J. Colloid Interface Sci.*, 2023, **633**, 851-865.
62. R. Song, Z. Zhong and L. Lin, *Int. J. Biol. Macromol.*, 2016, **85**, 102-110.
63. F. Luan, L. Wei, J. Zhang, W. Tan, Y. Chen, F. Dong, Q. Li and Z. Guo, *Molecules*, 2018, **23**, 516.
64. Y. Wu, Q. Wu, X. Fan, L. Yang, L. Zou, Q. Liu, G. Shi, X. Yang and K. Tang, *J. Biomed. Mater. Res. -A*, 2024, **112**, 1532-1547.
65. M. Yin, S. Wan, X. Ren and C.-C. Chu, *ACS Appl. Mater. Interfaces*, 2021, **13**, 14688-14699.
66. J. Preet, K. Pathania, J. Kaur, R. Singh, D. B. Salunke and S. V. Pawar, *Mater. Adv.*, 2024, **5**, 9445-9457.
67. Z. Li, X. Fan, Z. Luo, X. J. Loh, Y. Ma, E. Ye, Y.-L. Wu, C. He and Z. Li, *Nanoscale*, 2022, **14**, 14970-14983.
68. J. Lin, S. Li, Y. Ying, W. Zheng, J. Wu, P. Wang and X. Liu, *ACS Omega*, 2024, **9**, 4386-4394.
69. P. Jayabal, V. Kannan Sampathkumar, A. Vinothkumar, S. Mathapati, B. Pannerselvam, S. Achiraman and G. D. Venkatasubbu, *ACS Appl. Bio Mater.*, 2023, **6**, 615-627.
70. P. Heydari, A. Zargar Kharazi and L. Shariati, *Sci. Rep.*, 2024, **14**, 12019.

View Article Online
DOI: 10.1039/D5TB00800J

Data Availability Statement

Data available within the article or its supporting information.